1 **Enhanced O_2^+ Loss at Mars due to an Ambipolar Electric Field**

2 **from Electron Heating**

3 R. E. Ergun[1,2], L. A. Andersson[2], C. M. Fowler[1,2], A. K. Woodson[2], T. D. Weber[2], G. T.

4 Delory[3], D. J. Andrews[4], A. I. Eriksson[4], T. McEnulty[2], M. W. Morooka[2], A. I. F.

5 Stewart[2], P.R. Mahaffy[5], and B. M. Jakosky[2]

6 _____

7 Corresponding author: Robert E. Ergun, Laboratory of Atmospheric and Space Sciences,

8 University of Colorado, Boulder, Colorado, USA 80303. ree@lasp.colorado.edu.

9

10 [1]Department of Astrophysical and Planetary Sciences, University of Colorado, Boulder,

11 Colorado, USA.

12 [2]Laboratory of Atmospheric and Space Sciences, University of Colorado, Boulder,

13 Colorado, USA

14 [3]Space Sciences Laboratory, University of California, Berkeley, California, USA

15 [4]Swedish Institute of Space Physics (Uppsala), Uppsala, Sweden

16 [5]Planetary Environments Laboratory, Code 699, NASA Goddard Space Flight Center,

17 Greenbelt, MD.

18

19 **Key Points:**

20 Enhanced O_2^+ loss at Mars

21 Ambipolar electric field at Mars

Abstract

Recent results from the MAVEN Langmuir Probe and Waves (LPW) instrument suggest higher than predicted electron temperatures (T_e) in Mars' dayside ionosphere above ~180 km in altitude. Correspondingly, measurements from Neutral Gas and Ion Mass Spectrometer (NGIMS) indicate significant abundances of O_2^+ up to ~500 km in altitude, suggesting that O_2^+ may be a principal ion loss mechanism of oxygen. In this article, we investigate the effects of the higher T_e (which results from electron heating) and ion heating on ion outflow and loss. Numerical solutions show that plasma processes including ion heating and higher T_e may greatly increase O_2^+ loss at Mars. In particular, enhanced T_e in Mars' ionosphere just above the exobase creates a substantial ambipolar electric field with a potential ($e\Phi$) of several $k_B T_e$, which draws ions out of the region allowing for enhanced escape. With active solar wind, electron and ion heating, direct O_2^+ loss could match or exceed loss via dissociative recombination of O_2^+. These results suggest that direct loss of O_2^+ may have played a significant role in the loss of oxygen at Mars over time.

1. Introduction

Spacecraft and lander observations have provided strong evidence that Mars once had surface water and an atmosphere that is now lost, entreating one of the most intriguing questions in planetary science: how did Mars loose its atmosphere and water? Isotopic ratios give evidence of substantial loss to space [*Pepin*, 1994] whereas present-day in-situ observations indicate on-going loss at rates that are substantially lower than that needed for the inferred atmosphere and water loss.

The combination of Mars' weak gravitational binding and photochemical and plasma processes may be central to explaining Mars' atmospheric loss. The present-day photochemical loss is dominated by dissociative recombination of O_2^+ [e. g. *McElroy*, 1972; *Rohrbaugh et al.*, 1979; *Barth*, 1985; *Nagy and Cravens*, 1988; *Fox and Hac*, 2009], which creates a hot O corona about Mars. This process is primarily limited by the solar UV intensity, which, by some estimates, could have been as much as five to ten times higher four billion years ago [*Bressan et al.*, 1993; *Ayres*, 1997; *Sackmann and Boothroyd*, 2003; *Lundin et al.*, 2007]. Even with enhanced UV, however, this process would be responsible for loss of less than 1 m of surface water from Mars over 4 Gyr [*Lillis et al.*, 2015].

In situ observations of ion fluxes indicate that present-day ion loss is a fraction of that from dissociative recombination [e. g., *Lundin et al.*, 2004; *Barabash et al.*, 2007]. Fluxes of O^+, O_2^+ and CO_2^+ have been measured in space and appear to be highly variable and often sporadic. Escape rates are difficult to quantify due to returning fluxes [e. g. *Brain et al.*, 2015]. Stronger fluxes have been associated with stronger solar wind

62 activity (e. g. velocity, energy flux, magnetic field strength), albeit the association is not

63 well understood and is a topic of current studies [e. g. *Lundin et al.*, 2004].

64   The role of O_2^+ in photochemical loss is well documented [*Hanson et al.*, 1977; more

65 references can be found in recent reviews, e.g. *Nagy et al.* 2004; *Witasse et al.*, 2008;

66 *Withers,* 2009]. O_2^+ dissociative recombination appears to be the major, present-day loss

67 mechanism. Recent spacecraft observations [*Kar et al.*, 1996; *Bougher et al.*, 2015]

68 indicate that direct loss of O_2^+ is less but significant. *Fox* [1997] suggested that O_2^+ might

69 be the major escaping ion if escape is at maximum rates. Interestingly, [*Kar et al.*, 1996]

70 indicated that O_2^+ escape could be supported at observed rates [*Lundin et al.*, 1989; 1990]

71 if given a 1 km/s acceleration at the top side of Mars' ionosphere. We intend to

72 demonstrate that an ambipolar electric field can provide such acceleration.

73   Recent measurements of the electron temperature (T_e) altitude profile [*Ergun et al.*,

74 2015] reveal higher values of T_e (~0.3 eV) in the dayside ionosphere above 200 km than

75 that predicted (~1 eV) by modeling [e. g. *Withers et al.*, 2014], supporting the early

76 observations of Viking at altitudes above ~200 km [*Hanson and Mantas*, 1988]. Several

77 numerical models [*Chen et al.*, 1978; *Choi et al.*, 1998; *Matta et al.*, 2014; *Withers et al.*,

78 2014; *Cui et al.*, 2015] have demonstrated that solar heating is insufficient to reproduce

79 the elevated T_e as observed by *Hanson and Mantas* [1988]. The elevated dayside T_e, now

80 confirmed, is not fully understood; an electron heating mechanism has not been

81 identified.

82   In this article, we focus on a major consequence of the elevated electron

83 temperatures; the ambipolar electric field that retains the electrons also accelerates ions

84 out of the ionosphere. We examine present day and past O_2^+ escape with an ambipolar

85　electric field using recent MAVEN observations to guide Combined Photochemistry and

86　Ion Tracing (CAPIT) simulations [*Andersson et al.*, 2010].

87　　　A critical region for photochemical loss is the region surrounding the exobase. An

88　exobase is defined for a particular species. Since we are examining several species, we

89　use the term "exobase" to describe the boundary between collision-dominated

90　photochemical processes (low altitude) and the higher-altitude ionosphere where plasma

91　processes appear to play a dominant role. Under this definition, the exobase at Mars is

92　between ~180 km and ~220 km in altitude, depending on species and the conditions of

93　the neutral atmosphere.

94　　　Photochemical reactions are most intense well below the exobase due to the high

95　density of the neutral atmosphere. In addition, ionization from UV fluxes is strongest

96　below the exobase. Mars' atmosphere is optically thin above ~160 km. However,

97　photochemical interactions at low altitudes primarily influence the local ion constituency.

98　For example, at ~160 km in altitude, the mean free path of O_2^+ is less than 1 km so the

99　products of photochemical reactions remain localized and do not directly result in escape.

100　On the other hand, ions or energized neutrals that are created from photochemical

101　reactions above the exobase are free to travel long distances. However, the rapidly

102　decreasing density of the neutral atmosphere greatly reduces the ion production rates and

103　other photochemical reaction rates above the exobase. As a result, the region surrounding

104　the exobase (within a few scale heights) is critical to ion loss.

105　　　The CAPIT code focuses on this region. We use the CAPIT code to demonstrate that

106　the ambipolar electric field created through elevated electron temperatures (electron

107　heating) may be responsible for enhanced, present-day O_2^+ loss. Furthermore, under

108 extreme solar conditions, O_2^+ loss can exceed loss of oxygen via dissociative

109 recombination of O_2^+ by more that an order of magnitude. Therefore, it is possible that

110 direct O_2^+ loss may have played an important role in the loss of oxygen at Mars.

111   There are a plethora of processes that can influence ion escape. For example, the

112 magnetic field [*Acuna et al.*, 1998; 1999] near the exobase can play a critical role [e.g.,

113 *Hanson and Mantas*, 1988; *Choy et al.*, 1998; *Krymskii et al.*, 2003; *Duru et al.*, 2006;

114 *Lillis et al.*, 2011; *Matta et al.*, 2015]. A horizontal magnetic field binds ions and

115 electrons to the altitude at which they were created. At Mars, the draped magnetic field is

116 expected to have a small flare angle that directs ion flow from the dayside to the night

117 side with a slow rise in altitude. This long escape path causes ions to dwell in the

118 ionosphere for long periods increasing the possibility of recombination or subsequent

119 photochemical processes, thus reducing escape.

120   The composition of the neutral atmosphere can influence oxygen escape. For

121 example, the ratio of O to CO_2 densities influences O_2^+ production. The state of the solar

122 wind, its wave activity, the electric field penetration into the ionosphere, and the ionizing

123 fluxes of electrons and ions also can influence escape. In this article, we concentrate on

124 photochemical processes and plasma processes in the region surrounding the exobase to

125 understand the controlling factors in this region.

126 **2. MAVEN Observations**

127   MAVEN observations from the Langmuir Probe and Waves (LPW) instrument

128 [*Andersson et al.*, 2015; *Ergun et al.*, 2015] and the Neutral Gas and Ion Mass

129 Spectrometer (NGIMS) [*Mahaffy et al.*, 2015b] are displayed with CAPIT simulations in

130 both panels of Figure 1. The CAPIT simulations are discussed below. The MAVEN data

131   have been previously published [*Ergun et al.*, 2015; *Lillis et al.*, 2015; *Brougher et al.*,

132   2015], so our description is brief. Observations are from April 17, 2015 to April 22, 2015

133   during a "deep dip" campaign when MAVEN probed to altitudes just below 130 km with

134   low solar zenith angle, less than 15° at the lowest altitudes [see *Ergun et al.*, 2015 for

135   orbital coverage]. The solar UV intensity was moderate and the solar wind activity was

136   moderate.

137   Figure 1 (left) displays the altitude profile of the electron density (black circles with

138   error bars) derived from the LPW observations and averaged over the inbound part of

139   twenty-two orbits during a deep dip campaign [*Ergun et al.*, 2015]. By comparison with

140   electron density (n_e) determined by wave sounding [*Andersson et al.*, 2015], the LPW n_e,

141   at the lowest altitudes, is estimated to be within -25% to + 10% as indicated by the error

142   bars. At low altitudes, below ~180 km, n_e measurements are fairly repeatable from orbit

143   to orbit. Within an orbit, there was small variation. Above ~300 km in altitude, the n_e

144   variations are very strong, occasionally over an order of magnitude from orbit to orbit

145   and within an orbit. These data reflect the expectation that photochemical processes

146   dominate n_e below ~180 km, which leads to low variability, whereas plasma processes

147   appear to be active above that altitude leading to higher variability.

148   The green circles represent the O_2^+ density as measured by the NGIMS instrument

149   [*Mahaffy et al.*, 2015b]. The blue circles represent the O^+ density and the red circles

150   represent the CO_2^+ density. The NGIMS observations are the average density over the

151   same inbound legs of the twenty-two orbits during the deep-dip campaign. NGIMS has

152   excellent relative accuracy but requires a baseline for absolute accuracy. NGIMS

153   densities best correspond to the LPW densities if adjusted higher by a factor of ~1.5 for

154   all species. The adjustment is not applied in Figure 1. The good qualitative agreement of

155   the altitude profiles between LPW and NGIMS (total density) gives confidence that the

156   observations reflect the average structure of Mars' ionosphere. The NGIMS observations

157   also show the same variation pattern as the LPW observations: relatively low variation

158   below ~180 km and very strong variation above ~300 km. The observations show

159   enhanced O_2^+ densities at high altitude, that is the high-altitude densities are well above

160   standard scale-height expectations, supporting earlier observations from the Phobos 2

161   mission [e. g. *Kar et al.*, 1996] and photochemical models [e. g. *Fox*, 1997].

162   The measured electron temperature (T_e) profile from MAVEN LPW displayed in

163   Figure 1 right shows enhanced temperatures (~0.3 eV) from that predicted by

164   photochemical models at ~0.1 eV [*Chen et al.*, 1978; *Choi et al.*, 1998; *Matta et al.*,

165   2014; *Withers et al.*, 2014], indicating an electron energy source. One possibility is that

166   the electron energy may come from plasma wave heating. Alternatively, the enhanced T_e

167   may be due to transport of hot, shocked solar wind electrons to the ionosphere. The high-

168   altitude (above the exobase) T_e observations are in good agreement with T_e measured by

169   the Viking 1 lander [*Hanson and Mantas*, 1988].

170   The high values of T_e in the exobase region have several important consequences. An

171   ambipolar electric field with a potential ($e\Phi$) on the order of several times $k_B T_e$ is

172   required to retain the electrons. This same electric field will energize ions in the exobase

173   region and draw them into the upper ionosphere. For example, an ambipolar potential of

174   ~0.6 V will allow an O_2^+ ion at ~200 km to overcome gravitational potential and travel up

175   to ~1000 km in altitude. Once drawn out the exobase region, photochemical loss and

176   recombination are dramatically lowered due to the lower densities and higher T_e. Ion

177 heating through plasma waves can act to add energy to these ions so the likelihood of

178 escape can dramatically increase.

179 **3. CAPIT Model**

180 Several models have included higher T_e and the ambipolar potential either via a fluid

181 approach [e.g. *Fox*, 1997 and citations within], MHD models [e. g. *Ma et al.* 2002; 2014,

182 and citations within], or with hybrid models [e.g. *Brecht and Ledvina*, 2014 and citations

183 within]. The hybrid approaches have course altitude resolution (> 10 km) restricting the

184 accuracy in the exobase region. The CAPIT code is specifically designed to focus on the

185 exobase and accurately trace ions.

186 The 2D CAPIT model is described by *Andersson et al.*, [2010]. We use a 1D version

187 of CAPIT, which produces comparable results but allows for faster convergence and self-

188 consistent treatment of low-frequency Poynting flux that heats ions. In this section, we

189 briefly describe the CAPIT code and focus on the differences between the 1D CAPIT

190 code and the previously published 2D CAPIT code [*Andersson et al.*, 2010].

191 The basic idea behind the CAPIT model is to examine the critical layer of the dayside

192 ionosphere near the exobase. The CAPIT code simulates photochemical reactions on a

193 grid while tracing ions in space. The neutral densities are prescribed and remain constant;

194 they are not altered by photochemical reactions. The altitude profiles for CO_2, O, N_2, O_2,

195 NO, CO in this article have a density with a constant scale height derived from those in

196 *Mahaffy et al.*, [2015a] and *Lillis et al.*, [2015], which are based on NGIMS observations

197 during the same deep dip period that we examine.

198 Figure 2 shows the basic domain of the 1D CAPIT and 2D CAPIT codes. The 2D

199 CAPIT code includes an extended region along the draped magnetic field (blue region in

200   Figure 2). The 1D CAPIT code emulates this draped magnetic field line starting at low

201   solar zenith angle from low altitude (160 km in this article) to the top of the ionosphere

202   (500 km in this article) where solar wind phenomena begin to dominate. CAPIT 1D uses

203   a constant 10° (from horizontal) flare angle for the draped magnetic field. It allows for

204   motion along the draped field line but does not allow for variation of densities or other

205   parameters in the horizontal direction. Ion motion and the ambipolar electric field are

206   restricted to be along the magnetic field. Ion motion is controlled by the electric field,

207   magnetic field, plasma wave heating, gravity, and collisions.

208   The CAPIT code includes twenty-eight photochemical reactions relevant to the region

209   above the primary ionosphere density peak (M2 peak, which is at ~130 km in altitude),

210   detailed in Table 1. This set of interactions is expanded from that used by *Andersson et*

211   *al*., [2010] to include NO^+ and CO^+. CAPIT does not include UV absorption, so it is

212   primarily valid above ~160 km in altitude, where UV absorption is small. The mean free

213   path of ions at ~160 km is less than 1 km, so it is adequate to simulate the upper part of

214   the collisional ionosphere beginning at 160 km.

215   Both versions of the CAPIT code, 1D and 2D, have photoionization that operates in a

216   grid. The grid point in the 1D code spans 1 km in altitude, which is 5.75 km along a field

217   line (consistent with 10° flare angle). Every second, ions are created via random number

218   based on the neutral densities, photoionization rates, and solar UV flux in each grid. The

219   positions of ions within a grid are randomized and the velocities (parallel and

220   perpendicular to the magnetic field) are also randomized to mimic a distribution at the

221   same temperature as the neutral species that was ionized (300 ^{o}K for simulations in this

222   article). Once an ion is created, its motion is determined by the electric field, the

223 magnetic field, gravity, wave heating, and collisions. Ions also undergo a set of

224 photochemical interactions at the rates describe in Table 1, again at a one second

225 cadence. The hot O products from dissociative recombination of O_2^+ are assigned an

226 escape probability as a function of altitude to tabulate total loss via that process. The

227 neutral density of O, however, is not changed.

Table 1: Photochemical Reactions used in 1D CAPIT

Reaction (Ionization)	Rate (s^{-1}) Moderate Sun	Reference
$N_2 + \gamma \rightarrow N_2^+ + e^-$	2.80×10^{-7}	*Huebner et al.*, 1992
$CO_2 + \gamma \rightarrow CO_2^+ + e^-$	5.30×10^{-7}	*Huebner et al.*, 1992
$O + \gamma \rightarrow O^+ + e^-$	2.00×10^{-7}	*Huebner et al.*, 1992
$O_2 + \gamma \rightarrow O_2^+ + e^-$	4.40×10^{-7}	*Huebner et al.*, 1992
$NO + \gamma \rightarrow NO^+ + e^-$	10.1×10^{-7}	*Huebner et al.*, 1992
$CO + \gamma \rightarrow CO^+ + e^-$	3.44×10^{-7}	*Huebner et al.*, 1992

Reaction (Electron)	Rate (cm^3/s)	Reference
$N_2^+ + e^- \rightarrow N + N$	$2.2 \times 10^{-7} (300/T_e)^{0.39}$	*Matta*, 2013
$CO_2^+ + e^- \rightarrow CO + O$	$4.2 \times 10^{-7} (300/T_e)^{0.75}$	*Matta*, 2013
$O^+ + e^- \rightarrow O$ (not included)	$3.26 \times 10^{-12} (300/T_e)^{0.7}$	*Matta*, 2013
$O_2^+ + e^- \rightarrow 2O$ (see note)	$2.4 \times 10^{-7} (300/T_e)^{0.7}$	*Matta*, 2013
$NO^+ + e^- \rightarrow NO$	$4.0 \times 10^{-7} (300/T_e)^{0.5}$	*Schunk and Nagy*, 2009
$CO^+ + e^- \rightarrow NO$	$2.75 \times 10^{-7} (300/T_e)^{0.55}$	*Schunk and Nagy*, 2009

Reaction	Rate at 300 ^oK (cm^3/s)	Reference
$N_2^+ + O \rightarrow O^+ + N_2$	9.8×10^{-12}	*Matta*, 2013
$N_2^+ + O \rightarrow NO^+ + N$	1.3×10^{-10}	*Matta*, 2013
$N_2^+ + NO \rightarrow NO^+ + N_2$	4.1×10^{-10}	*Schunk and Nagy*, 2009
$N_2^+ + O_2 \rightarrow O_2^+ + N_2$	5.0×10^{-11}	*Schunk and Nagy*, 2009
$N_2^+ + CO_2 \rightarrow O_2^+ + N_2$	8.0×10^{-10}	*Matta*, 2013
$CO^+ + O \rightarrow O^+ + CO$	1.4×10^{-10}	*Schunk and Nagy*, 2009
$CO^+ + CO_2 \rightarrow CO_2^+ + CO$	1.1×10^{-9}	*Schunk and Nagy*, 2009
$CO_2^+ + O \rightarrow O^+ + CO_2$	9.6×10^{-11}	*Matta*, 2013
$CO_2^+ + O \rightarrow O_2^+ + CO$	1.6×10^{-10}	*Matta*, 2013
$CO_2^+ + NO \rightarrow NO^+ + CO_2$	1.23×10^{-10}	*Schunk and Nagy*, 2009
$CO_2^+ + O_2 \rightarrow O_2^+ + CO_2$	5.0×10^{-11}	*Barth*, 1985
$O^+ + N_2 \rightarrow NO^+ + N$	1.2×10^{-12}	*Matta*, 2013
$O^+ + O_2 \rightarrow O_2^+ + O$	2.1×10^{-11}	*Schunk and Nagy*, 2009
$O^+ + NO \rightarrow NO^+ + O$	8.0×10^{-13}	*Schunk and Nagy*, 2009
$O^+ + CO_2 \rightarrow O_2^+ + CO$	1.1×10^{-9}	*Matta*, 2013
$O_2^+ + NO \rightarrow NO^+ + O_2$	4.6×10^{-10}	*Schunk and Nagy*, 2009

228

229   Ion motion is traced along a field line that is 10° from parallel to the surface. CAPIT

230   1D assumes a magnetic mirror ratio of 1.33 between 160 km and 500 km, corresponding

231   to a reduction in strength of a factor of 0.75 in magnetic field. The mirror force is applied

232   at each time step using the perpendicular velocity of the ion, altering the parallel and

233   perpendicular velocity. The full gyration of the ion is not traced in the 1D code. The

234   Collisions are treated as described in *Andersson et al.*, [2010]. Breifly, at each time step

235   and for each ion, a random number is called and weighted with the neutral densities to

236   determine if an ion is to undergo a collision. If a collision is called for, a neutral particle

237   is created with a random velocity (speed and direction) consistent with the neutral

238   temperature (300 ^{o}K). The impact parameter and azimuthal angle of the collision are also

239   generated randomly. The ion-neutral collision acts to conserves momentum and energy

240   and the ion is assigned a new velocity and direction in accordance to the collision. The

241   neutral particle is then discarded, as there is no change in neutral densities and

242   temperatures.

243   Wave heating is self-consistently implemented via a low-frequency Poynting flux

244   introduced at the upper boundary [*Ergun et al.*, 2008; *Andersson et al.*, 2010]. The wave

245   heating increases the perpendicular ion velocity; it does not directly affect the parallel

246   velocity. The Poynting flux is depleted as it heats ions, conserving energy. This energy

247   balance has an interesting effect as noted by *Andersson et al*. [2010]. The Poynting flux

248   heats ions, which, through the mirror force, accelerates ions to higher altitudes. The

249   enhanced ion densities at higher altitudes, in turn, absorb the Poynting flux before it

250   reaches lower altitudes. This effect limits the how much Poynting flux can enhance

251   outflow.

252   The electron temperature profile is prescribed in the 1D CAPIT code (Figure 1, right).

253   The analytic formula is taken from *Ergun et al.*, [2015]:

254

$$T_e = \frac{T_{eH} + T_{eL}}{2} + \frac{T_{eH} - T_{eL}}{2} \tanh\left(\frac{z - Z_o}{H_o}\right)$$

(1)

255

256   T_{eL}, the asymptotic value of T_e at the lowest altitudes, is set to 0.044 eV (510 ^{o}K). T_{eH} is

257   the high-altitude asymptotic value of T_e, which is set to 0.271 eV (3140 ^{o}K). Z_o is set to

258   241 km. It represents the altitude of the most rapid change in T_e. Finally H_o , the scale

259   height of the rapid change is set to 60 km. The fit is plotted in Figure 1 (right).

260   The ambipolar electric field (potential) is derived from the T_e and n_e profiles. The

261   electron force equation parallel to the magnetic field and under equilibrium is [e.g.

262   *Schunk and Nagy*, 2009; *Hartle and Grebowsky*, 1995]:

263

$$eE = -\partial P_e / \partial s$$

(2)

264

265   where $P_e = n_e k_B T_e$ is the electron pressure, e is the fundamental charge, s is coordinate in

266   direction of the magnetic field, and k_B is the Boltzmann constant. In the 1 D CAPIT code,

267   E is calculated from the derivative of a smoothed n_e and the assigned T_e profile. The

268   electron density is derived from the ion density assuming a quasi-neutral plasma. The

269   electric field is assumed to be along the magnetic field.

270   Outflow rates of the ions are estimated from transport at the high-altitude boundary of

271   the simulation domain (500 km). Ions that pass through the boundary with sufficient

272   kinetic energy to overcome gravitational binding are considered to have escaped; the flux

273 is designated as F_{min}. While it is possible that a fraction of these ions may return to the

274 night-side ionosphere, we do not attempt to correct for such return flows, which may lead

275 to an overestimate of the minimum escape. On the other hand, the majority of ions

276 passing through the high-altitude boundary often do not have sufficient kinetic energy for

277 escape. If the kinetic energy is such that the ion will return before reaching the terminator

278 (~700 km in altitude; see Figure 1), its velocity is reversed and it reenters the simulation

279 domain.

280   The remaining ions that pass through the high-altitude boundary, those with

281 insufficient kinetic energy to overcome gravitational binding, may escape with additional

282 heating or acceleration by the solar wind electric field. The escape probability of these

283 ions leads to the largest uncertainty in our results. We assign the maximum outflow rate

284 (F_{max}) as all ions passing through the high-altitude boundary with sufficient energy to

285 reach the terminator (700 km in altitude, see Figure 2). We generate an "estimated"

286 escape flux by assigning an escape probability (P) based on the kinetic energy (KE) of

287 the outgoing ion and its gravitational binding energy ($W_{Gravity}$):

288

$$P = \frac{KE}{W_{Gravity}}, KE < W_{Gravity}; \ P = 1, KE \geq W_{Gravity} \tag{3}$$

289

290   F_{Est}, the estimated escape flux, is complied by summing over the escape probabilities

291 of all escaping ions. F_{Est} is ploted the nominal outflow rate. The escape probabilities are

292 set so that estimated outflow rates from 1D CAPIT are similar to those predicted by 2D

293 CAPIT and other models [e.g. *Fox*, 1997 and citations within]. The escape rates from 1D

294 CAPIT are also within an order of magnitude of those estimated through measurements

295 [e. g. *Lundin et al.*, 2004; Barabash *et al.*, 2007; Brain et al., 2015], we emphasize that, as

296 with most modeling efforts, there is a significant quantitative uncertainly in determining

297 escaped fluxes. The major conclusions of this article are based on the qualitative

298 properties of the outflow.

299 **4. Results**

300 Figure 1 (left) displays results from CAPIT code as solid lines. The electron density is

301 black, O_2^+ is green, O^+ is blue and CO_2^+ is red. The neutral O density was increased (by

302 ~1.4) from that reported by Mahaffy et al. [2015a] and the low-frequency Poynting flux

303 (ion heating) was adjusted to 3.16×10^{-8} W/m^2 to obtain agreement between CAPIT and

304 observations. Considering that the observations are averaged over 28 orbits, we find that

305 the CAPIT results are in excellent qualitative agreement with the observed altitude

306 profiles with quantitative differences, for the most part, less than a factor of 2. The

307 primary differences are at high altitudes (>200 km); CAPIT predicts slightly higher than

308 observed densities of both O^+ and O_2^+, but has excellent quantitative agreement with the

309 LPW density. The NGIMS densities (O_2^+, O^+, and CO_2^+), however, were not adjusted to

310 match the LPW electron density. Some difference is therefore expected.

311 The differences between the CAPIT results and NGIMS observations below ~200 km

312 are from several factors. Since CAPIT does not have UV absorption, it predicts higher

313 CO_2 ionization. The O^+ density profile at low altitudes is sensitive to the density profile

314 of O, which is modeled from a single scale height whereas observations show a more

315 complex structure. The O density profile also influences the O_2^+ density profile.

316 One of the most significant features of the 1D CAPIT model is its ability to examine

317 the impact of the electron temperature profile on ion outflow. The ambipolar electric

318   field, which retains the electrons, will accelerate ions along a magnetic field to higher

319   altitudes. Figure 3 (left) displays the outflow rates as a function of high-altitude electron

320   temperature (T_{eH} in Equation 1) with weak low-frequency Poynting flux of 3.16×10^{-10}

321   W/m^2. The colors represent species: purple is the estimated O outflow from dissociative

322   recombination of O_2^+, blue is O^+ outflow, green is O_2^+ outflow, and red is CO_2^+ outflow.

323   The dashed lines show the maximum (F_{max}) and minimum (F_{min}) outflow rates as

324   described in section 3.

325   There are several salient features in Figure 3 left. One can see a dramatic increase in

326   the estimated O_2^+ outflow rates with increasing T_{eH}. F_{max} of O_2^+ increases to that of O^+,

327   nearly three orders of magnitude with the increase in T_{eH}. F_{min}, however, does increase

328   but remains low indicating that most O_2^+ ions leaving the simulation domain do not have

329   escape energy. Additional energy is needed for escape. It is clear that the ambipolar

330   electric field rapidly draws O_2^+ from below the exobase (~200 km) to higher altitudes

331   into a collisionless environment reducing recombination loss and dramatically increasing

332   the possible direct ion outflow. CO_2^+ is also drawn out, but at significantly lower fluxes.

333   Estimated and maximum O^+ outflow is increased, but not as dramatically as O_2^+. O^+ is

334   created at higher altitudes with peak densities above 250 km (Figure 1, left), which is

335   already well above the exobase.

336   The right panel of Figure 3 displays outflow as a function of T_{eH} with nominal low-

337   frequency Poynting flux (3.16×10^{-8} W/m^2). Ion heating dramatically raises F_{max} at low

338   values of T_{eH}. The results suggest that either ion heating or higher electron temperatures

339   can increase possible outflow.

340   Figure 4 displays why both T_e and Poynting flux both must be considered when

341   studying outflow. The left panel of Figure 4 displays estimated outflow as a function of

342   low-frequency Poynting flux (ion heating rate) under a low T_{eH} (0.044 eV), and therefore

343   a low ambipolar electric field. These results agree with those in *Andersson et al.*, [2010],

344   who, using a 0.1 eV constant T_e, showed increasing O^+ and O_2^+ outflow with ion heating.

345   In particular F_{max} of O_2^+ increases dramatically, allowing for possible larger escape.

346   Figure 4 (right) displays a less intense increase in outflow when T_{eH} is set at the recently

347   measured value (0.271 eV). The primary difference between the two plots comes from

348   the stronger ambipolar electric field in the right plot, whereas the left plot, similar to that

349   in *Andersson et al.* [2010], has a weak ambipolar electric field.

350   The estimated O outflow from dissociative recombination (purple squares) decreases

351   with increasing T_{eH} and decreases with increasing Poynting flux. The decrease in

352   dissociative recombination is due in part to the increase in T_{eH} but primarily from

353   transport of O_2^+ out of the region near the exobase. Interestingly, the decrease in

354   dissociative recombination appreciably offsets the increased outflow of oxygen atoms

355   from ion outflow. In other words, the increase in O_2^+ outflow comes partly at the expense

356   of dissociative recombination of O_2^+.

357   **5. Discussion and Past Outflow**

358   The primary result from the simulations, constrained by MAVEN observations, is the

359   strong sensitivity of O_2^+ outflow, in particular F_{max}, to the ambipolar electric field. The

360   Poynting fluxes of low frequency plasma waves also increase outflow of all species as

361   reported earlier [*Andersson et al.,* 2010]. These results demonstrate at least two

362   mechanisms in which ion heating or electron heating, presumably linked to increased

363   solar wind activity, can enhance ion outflow.

364   The increased T_{eH} requires an energy source for electrons [e.g. *Schunk and Nagy*,

365   2009]. Modeling efforts [e.g. *Matta et al.*, 2014] predict that T_e is close to the neutral

366   temperature (~0.026 eV) below ~125 km in altitude but rises quickly with altitude to ~0.1

367   eV. For $T_{eH} \sim 0.3$ eV, a heat source is required [*Chen et al.*, 1978; *Choi et al.*, 1998;

368   *Matta et al.*, 2014; *Withers et al.*, 2014; *Cui et al.*, 2015]. Furthermore, the ambipolar

369   electric field is energizing ions, so a continuous energy source into the electrons is

370   required. One possibility is plasma wave heating in the topside ionosphere [e. g. *Ergun et*

371   *al.*, 2006; *Schunk and Nagy*, 2009; *Andersson et al.*, 2010]. Another possibility is that

372   hot, shocked solar wind electrons are transported into the topside ionosphere.

373   The early sun, roughly 4 Gyr ago, is estimated to have ~70% less luminosity but

374   significantly higher output in ionizing radiation (in particular, UV) and significantly more

375   energetic solar wind [*Bressan et al.*, 1993; *Ayres*, 1997; *Sackmann and Boothroyd*, 2003].

376   Fluxes of ionizing radiation are expected to be roughly five times the present day rate

377   while the solar wind speed could be up to an order of magnitude higher. Solar wind

378   forcing could enhance atmospheric escape in a variety of ways including penetration of

379   the solar wind electric field, sputtering, and enhanced ion outflow [e. g. *Lundin et al.*,

380   2007].

381   Focusing on the critical region near the exobase, it is clear that a combination of

382   increased photochemical production of ions and increased escape efficiency could greatly

383   enhance escape. Figure 5 shows outflow rates as a function of enhanced solar activity

384   using the present-day neutral atmosphere. In this figure, the solar UV flux (F_{UV}) is plotted

385   linearly. However, the solar wind energy flux is expected to increase more than linearly

386   [*Lundin et al.*, 2007]. We increase the low-frequency Poynting flux as F_{UV}^2 assuming a

387   linear increase in solar wind velocity and that the wave energy is proportional the solar

388   wind energy flux. It is entirely possible that the solar wind density and magnetic field

389   strength also increase, further increasing the solar wind energy flux. An increase in wave

390   energy would increase the electron temperature as well. However, radiative cooling and

391   other losses would limit the increase in T_e, so T_{eH} is increased as $F_{UV}^{1.5}$ whereas T_{eL} is

392   increased linearly. The increases in T_e are not justified further and would be very difficult

393   to rigorously defend. We present the estimated outflow rates with the given values of

394   solar UV, Poynting flux, T_{eH} , and T_{eL} , which is one possible scenario that we

395   investigate.

396   The color scheme in Figure 5 is identical to that in Figures 3 and 4. The horizontal

397   axis shows the solar UV flux linearly, the Poynting flux, T_{eH}, and T_{eL}. The left panel has a

398   magnetic field at 10° from horizontal; the right panel has a vertical magnetic field. At

399   high solar UV fluxes and high solar wind forcing, the outflow of ions exceeds that of

400   dissociative recombination by roughly an order of magnitude. F_{min} and F_{max} are nearly

401   identical at high UV (high T_e) indicating that most O^+, O_2^+, and CO_2^+ ions that leave the

402   simulation domain have escape energy. If T_{eH} exceeds ~1 eV, the ambipolar electric field

403   can accelerate O_2^+ atoms to escape velocity.

404   With a 10° from horizontal magnetic field, the net outflow rate reaches ~10^{13} oxygen

405   Atoms/m^{2}s (~3.3x10^{26} Atom/s globally). This outflow rate can remove roughly 2 m of

406   water in ~1 Gyr. The outflow rate is roughly four to five times higher if the magnetic

407 field is vertical. These results suggest that it is possible that ion outflow could have

408 caused significant water or atmospheric loss at Mars.

409   There are many caveats to the simulations of the past outflow rates. The composition

410 of the neutral atmosphere was certainly dissimilar to the present-day composition. The

411 magnetic field structure has also dramatically changed. The solar UV flux and solar

412 forcing parameters, while reasonable estimates with current knowledge, may have been

413 substantially different. As such, our primary conclusions must be limited to the present-

414 day exobase and the role of the ambipolar electric field.

415 **6. Conclusions**

416   CAPIT simulations focused on the exobase region and constrained by MAVEN

417 observations, show that the ambipolar electric field from heated electrons can

418 substantially increase ion outflow (O^+, O_2^+, and CO_2^+) in the present day. The maximum

419 outflow rates increase dramatically, but additional energy is needed for escape. Our

420 primary conclusion is that the combination of ion heating (low-frequency Poynting flux)

421 and acceleration by the ambipolar electric field draws O^+, O_2^+ and CO_2^+ from the exobase

422 and can dramatically enhance ion outflow, in particular, outflow of O_2^+.

423   We demonstrated a dramatic increase of ion outflow with electron heating and ion

424 heating processes under stronger solar UV and solar wind forcing. Direct ion outflow

425 exceeded that of dissociative recombination of O_2^+. It is possible, then, that ion outflow

426 could have been a significant factor in the loss of Mars' water and atmosphere.

427

Acknowledgments

References

Acuna, M. H., et al. (1998), Magnetic field and plasma observations at Mars: Initial results of the Mars Global Surveyor mission, *Science*, 279, 1676–1680, doi:10.1126/science.279.5357.1676.

Acuna, M. H., et al. (1999), Global distribution of crustal magnetization discovered by the Mars Global Surveyor MAG/ER experiment, *Science*, 284, 790–793, doi:10.1126/science.284.5415.790.

Andersson, L., R. E. Ergun, and A. I. F. Stewart (2010), The combined atmospheric photochemistry and ion tracing code: Reproducing the Viking Lander results and initial outflow results, *Icarus*, 206, 120–129, doi:10.1016/j.icarus.2009.07.009.

449 Andersson, L., R. E. Ergun, G. Delory, A. I. Eriksson, J. Westfall, H. Reed, J. F. Mccauley,

450   D. J. Summers, and D. Meyers (2015), The Langmuir Probe and Waves Experiment for

451   MAVEN, *Space Science Reviews*.

452 Ayres, T. (1997), Evolution of the solar ionizing flux, J. Geophys. Res., 102, 1641–1651,

453   doi:10.1029/96JE03306.

454 Barabash, S., A. Fedorov, R. Lundin, and J. A. Sauvaud (2007), Martian atmospheric erosion

455   rates, *Science*, 315, 501–503, doi:10.1126/science.1134358.

456 Barth, C. A., 1985, The photochemistry of the atmosphere of Mars, In: Levine, J. S. (Ed.),

457   The photochemistry of atmospheres: Earth, the other planets, and comets, *Academic*

458   *Press*. Inc., Orlando, pp 337-392.

459 Brain, D. A., et al. (2015), The spatial distribution of planetary ion fluxes near Mars observed

460   by MAVEN, *Geophys. Res. Lett.*, 42, doi:10.1002/2015GL065293.

461 Bressan, A., F. Fagotto, G. Bertelli, C. Chiosi, (1993) Evolutionary sequences of stellar

462   models with new radiative opacities. II - Z = 0.02, *Astron. Astrophys*. Suppl. Ser. 100,

463   647–664.

464 Brecht, S. H., and S. A. Ledvina (2014), The role of the Martian crustal magnetic fields in

465   controlling ionospheric loss, *Geophys. Res. Lett.*, 41, 5340–5346,

466   doi:10.1002/2014GL060841.

467 Bougher, S., et al. (2015a), Early MAVEN deep dip campaign reveals thermosphere and

468   ionosphere variability, *Science*, 350(6261), 0459, doi:10.1126/science.aad0459.

469 Chaufray, J.-Y., F. Gonzalez-Galindo, F. Forget, M. Lopez-Valverde, F. Leblanc, R. Modolo,

470   S. Hess, M. Yagi, P.-L. Blelly, and O. Witasse (2014), Three-dimensional Martian

471   ionosphere model: II. Effect of transport processes due to pressure gradients, *J. Geophys.*

472   *Res. Planets*, 119, 1614–1636, doi:10.1002/2013JE004551.

473 Chen, R. H., T. E. Cravens, and A. F. Nagy (1978), The Martian ionosphere in light of the

474   Viking observations, *J. Geophys. Res.*, 83, 3871–3876, doi:10.1029/JA083iA08p03871.

475 Choi, Y. W., J. Kim, K. W. Min, A. F. Nagy, and K. I. Oyama (1998), Effect of the magnetic

476   field on the energetics of Mars ionosphere, *Geophys. Res.Lett.*, 25, 2753–2756,

477   doi:10.1029/98GL51839.

478 Cui, J., M. Galand, S. J. Zhang, E. Vigren, and H. Zou (2015), The electron thermal structure

479   in the dayside Martian ionosphere implied by the MGS radio occultation data. *J.*

480   *Geophys. Res. Planets*, 120, 278–286. doi: 10.1002/2014JE004726.

481 Duru, F., D. A. Gurnett, T. F. Averkamp, D. L. Kirchner, R. L. Huff, A. M. Persoon, J. J.

482   Plaut, and G. Picardi (2006), Magnetically controlled structures in the ionosphere of

483   Mars, *J. Geophys. Res.*, 111, A12204, doi:10.1029/2006JA011975.

484 Ergun, R. E., L. Andersson, W. K. Peterson, D. Brain, G. T. Delory, D. L. Mitchell, R. P.

485   Lin, and A. W. Yau (2006), Role of plasma waves in Mars' atmospheric loss, *Geophys.*

486   *Res. Lett.*, 33, L14103, doi:10.1029/2006GL025785.

487 Ergun, R. E.,M.W.Morooka, L. A. Andersson, C.M. Fowler, G. T. Delory, D. J. Andrews, A.

488   I. Eriksson, T. McEnulty, and B. M. Jakosky (2015), Dayside electron temperature and

489   density profiles at Mars: First results from the MAVEN Langmuir probe and waves

490   instrument, *Geophys. Res. Lett.*, 42, doi:10.1002/2015GL065280.

491 Fox, J. L. (1997), Upper limits to the outflow of ions at Mars: Implications for atmospheric

492   evolution, Geophys. Res. Lett., 24, 2901–2904, doi:10.1029/97GL52842.

493 Fox, J. L., and A. Hac (2009), Photochemical escape of oxygen from Mars: A comparison of

494   the exobase approximation to a Monte Carlo method, *Icarus*, 204, 527–544,

495   doi:10.1016/j.icarus.2009.07.05.

496 Haider, S. A., S. P. Seth, E. Kallio, and K. I. Oyama (2002), Solar EUV and electron-proton-

497   hydrogen atom-produced ionosphere on Mars: Comparative studies of particle fluxes and

498   ion production rates due to different processes, *Icarus*, 159, 18 – 30.

499 Hanson, W. B., S. Sanatani, and D. R. Zuccaro (1977), The Martian ionosphere as observed

500   by the Viking retarding potential analyzers, *J. Geophys. Res.*, 82, 4351–4363,

501   doi:10.1029/JS082i028p04351.

502 Hanson, W. B., and G. P. Mantas (1988), Viking electron temperature measurements:

503   Evidence for a magnetic field in the Martian ionosphere, *J. Geophys. Res.*, 93, 7538 –

504   7544.

505 Hartle, R. E., and J. M. Grebowsky (1995), Planetary loss from light ion escape on Venus,

506   Adv. Space Res., 15(4), 117 –122, doi:10.1016/0273-1177(94)00073-A.

507 Huebner, W. F., J. J. Keady, and S. P. Lyon (1992), Solar photo rates for planetary

508   atmospheres and atmospheric pollutants, *Astrophys. Space Sci.*, 195,1–294.

509 Kar, J., K. K. Mahajan, and R. Kohli (1996), On the outflow of O_2^+ ions at Mars, *J. Geophys.*

510   *Res.*, 101(E5), 12747–12752, doi:10.1029/95JE03526.

511 Krymskii, A. M., T. K. Breus, N. F. Ness, D. P. Hinson, and D. I. Bojkov (2003), Effect of

512   crustal magnetic fields on the near terminator ionosphere at Mars: Comparison of in situ

513   magnetic field measurements with the data of radio science experiments on board Mars

514   Global Surveyor, *J. Geophys. Res.*, 108(A12), 1431, doi:10.1029/2002JA009662.

515 Lillis, R. J., M. O. Fillingim, and D. A. Brain (2011), Three-dimensional structure of the

516   Martian nightside ionosphere: Predicted rates of impact ionization from Mars Global

517   Surveyor magnetometer and electron reflectometer measurements of precipitating

518   electrons, J. *Geophys. Res.*, 116, A12317, doi:10.1029/2011JA016982.

519 Lillis, R. J., et al. (2015), Characterizing atmospheric escape from Mars today and through

520   time, with MAVEN, *Space Sci. Rev.*, doi:10.1007/s11214-015-0165-8.

521 Lundin, R., et al. (1989), First measurements of the ionospheric plasma escape from Mars,

522   *Nature*, 341, 609 – 612.

523 Lundin, R ., A. Zakharov, R. Pellinen, S. W. Barabasj, H. Borg, E. M. Dubinin, B. Hultqvist,

524   H. Koskinen, I. Liede, and N. Pissarenko (1990), Aspera/Phobos measurements of the ion

525   outflow from the martian ionosphere, *Geophys. Res. Lett.*, 17, 873– 876.

526 Lundin, R., et al. (2004), Solar wind-induced atmospheric erosion at Mars: First results from

527   ASPERA-3 on Mars Express, Science, 305, 1933–1936.

528 Lundin, R., H. Lammer, and I. Ribas (2007), Planetary magnetic fields and solar forcing:

529   Implications for atmospheric evolution, Space Sci. Rev., 129(1–3), 245–278,

530   doi:10.1007/s11214-007-9176-4.

531 Ma, Y., A. F. Nagy, K. C. Hansen, and D. L. DeZeeuw (2002), Three-dimensional

532   multispecies MHD studies of the solar wind interaction with Mars in the presence of

533   crustal fields, *J. Geophys. Res.*, 107(A10), 1282, doi:10.1029/2002JA009293.

534 Ma, Y. J., X. Fang, A. F. Nagy, C. T. Russell, and G. Toth (2014), Martian ionospheric

535   responses to dynamic pressure enhancements in the solar wind, *J. Geophys. Res*. Space

536   390 Physics, 119, 1272–1286, doi:10.1002/2013JA019402

537 Matta, M. M. (2013), Modeling the Martian Ionosphere, PhD, Boston Univ., Boston, Mass.

538 Matta, M., M. Galand, L. Moore, M. Mendillo, and P. Withers (2014), Numerical simulations

539   of ion and electron temperatures in the ionosphere of Mars: Multiple ions and diurnal

540   variations, Icarus, 227, 78–88, doi:10.1016/j.icarus.2013.09.006.

541 Matta, M., M. Mendillo, P. Withers, and D. Morgan (2015), Interpreting Mars ionospheric

542   anomalies over crustal magnetic field regions using a 2-D ionospheric model, *J. Geophys.*

543   *Res. Space Physics*, 120, 766–777, doi:10.1002/2014JA020721.

544 Mahaffy, P. R., M. Benna, M. Elrod, R. V. Yelle, S. W. Bougher, S. W. Stone, and B. M.

545   Jakosky (2015a), Structure and composition of the neutral upper atmosphere of Mars

546   from the MAVEN NGIMS investigation, *Geophys. Res. Lett.*, 42, 8951–8957,

547   doi:10.1002/2015GL065329.

548 Mahaffy, P. R., et al. (2015b), The neutral gas and ion mass spectrometer on the Mars

549   Atmosphere and Volatile Evolution mission, *Space Sci. Rev.*, doi:10.1007/s11214-014-

550   0091-1.

551 Nagy A. F., D. Winterhalter, K. Sauer, T. E. Cravens, S. Brecht, C. Mazelle, D. Crider, E.

552   Kallio, A. Zakharov, E. Dubinin, M. Verigin, G. Kotova, W. I. Axford, C. Bertucci, and

553   J. G. Trotignon (2004), The plasma environment of Mars, *Space Sci. Rev.*, 111, 33-114,

554   doi:/10.1023/B:SPAC.0000032718.47512.92.

555 Nagy, A. F., and T. E. Cravens (1988), Hot oxygen atoms in the upper atmospheres of Venus

556   and Mars, *Geophys. Res. Lett.*, 15, 433-435.

557 Pepin, R.O., Evolution of the Martian Atmosphere, 1994. *Icarus*, 111, 289-304.

558 Rohrbaugh, R. P., J. S. Nisbet, E. Bleuler, and J. R. Herman (1979), The effect of

559   energetically produced O_2^+ on the ion temperatures of the Martian thermosphere, *J.*

560   *Geophys. Res.*, 84, 3327 − 3338.

561 Schunk, R. W. and Nagy, A. F., (2009) Ionospheres, 2nd Ed. Cambridge University Press,

562   Cambridge.

563 Sackmann, I. J., and A. I. Boothroyd (2003), Our Sun. V. A bright young Sun consistent with

564   helioseismology and warm temperatures on ancient Earth and Mars, *Ap. J.*, 583, 1024–

565   1039.

566 Witasse O., T. Cravens, M. Mendillo, J. Moses, A. Kliore, A. Nagy, and T. Breus (2008),

567   Solar System Ionospheres, *Space Sci. Rev.*, 139, 235-265, doi:/10.1007/s11214-008-

568   9395-3.

569 Withers, P. (2009), A review of observed variability in the dayside ionosphere of Mars, *Adv.*

570   *Space Res.*, 44, 277–307, doi:10.1016/j.asr.2009.04.027.

571 Withers, P., K. Fallows, and M. Matta (2014), Predictions of electron temperatures in the

572   Mars ionosphere and their effects on electron densities, Geophys. Res. Lett., 41, 2681–

573   2686, doi:10.1002/2014GL059683.

574

575

576

577

578

579

580

581

582

583

585 **Tables**

Table 1: Photochemical Reactions used in 1D CAPIT

Reaction (Ionization)	Rate (s^{-1}) Moderate Sun	Reference
$N_2 + \gamma \rightarrow N_2^+ + e^-$	2.80×10^{-7}	*Huebner et al.*, 1992
$CO_2 + \gamma \rightarrow CO_2^+ + e^-$	5.30×10^{-7}	*Huebner et al.*, 1992
$O + \gamma \rightarrow O^+ + e^-$	2.00×10^{-7}	*Huebner et al.*, 1992
$O_2 + \gamma \rightarrow O_2^+ + e^-$	4.40×10^{-7}	*Huebner et al.*, 1992
$NO + \gamma \rightarrow NO^+ + e^-$	10.1×10^{-7}	*Huebner et al.*, 1992
$CO + \gamma \rightarrow CO^+ + e^-$	3.44×10^{-7}	*Huebner et al.*, 1992

Reaction (Electron)	Rate (cm^3/s)	Reference
$N_2^+ + e^- \rightarrow N + N$	$2.2 \times 10^{-7} (300/T_e)^{0.39}$	*Matta*, 2013
$CO_2^+ + e^- \rightarrow CO + O$	$4.2 \times 10^{-7} (300/T_e)^{0.75}$	*Matta*, 2013
$O^+ + e^- \rightarrow O$ (not included)	$3.26 \times 10^{-12} (300/T_e)^{0.7}$	*Matta*, 2013
$O_2^+ + e^- \rightarrow 2O$ (see note)	$2.4 \times 10^{-7} (300/T_e)^{0.7}$	*Matta*, 2013
$NO^+ + e^- \rightarrow NO$	$4.0 \times 10^{-7} (300/T_e)^{0.5}$	*Schunk and Nagy*, 2009
$CO^+ + e^- \rightarrow NO$	$2.75 \times 10^{-7} (300/T_e)^{0.55}$	*Schunk and Nagy*, 2009

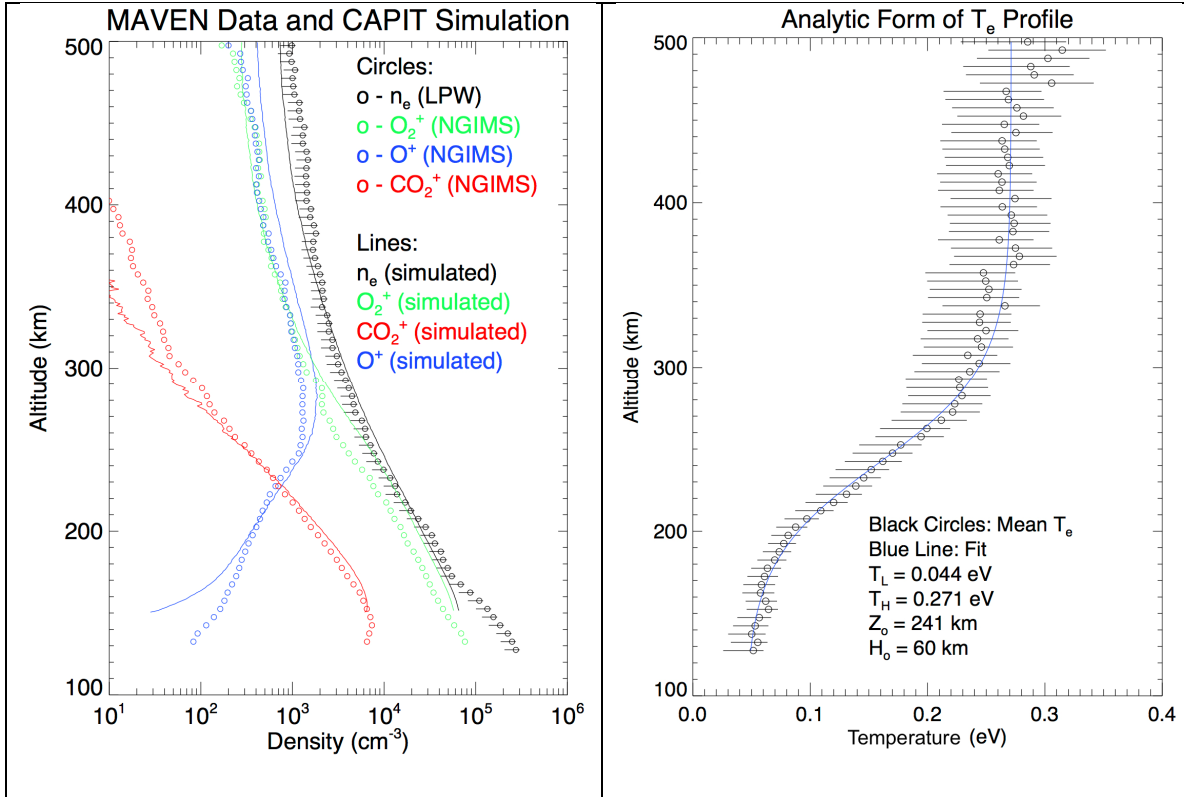| Reaction	Rate at 300 ^{o}K (cm^3/s)	Reference
$N_2^+ + O \rightarrow O^+ + N_2$	9.8×10^{-12}	*Matta*, 2013
$N_2^+ + O \rightarrow NO^+ + N$	1.3×10^{-10}	*Matta*, 2013
$N_2^+ + NO \rightarrow NO^+ + N_2$	4.1×10^{-10}	*Schunk and Nagy*, 2009
$N_2^+ + O_2 \rightarrow O_2^+ + N_2$	5.0×10^{-11}	*Schunk and Nagy*, 2009
$N_2^+ + CO_2 \rightarrow O_2^+ + N_2$	8.0×10^{-10}	*Matta*, 2013
$CO^+ + O \rightarrow O^+ + CO$	1.4×10^{-10}	*Schunk and Nagy*, 2009
$CO^+ + CO_2 \rightarrow CO_2^+ + CO$	1.1×10^{-9}	*Schunk and Nagy*, 2009
$CO_2^+ + O \rightarrow O^+ + CO_2$	9.6×10^{-11}	*Matta*, 2013
$CO_2^+ + O \rightarrow O_2^+ + CO$	1.6×10^{-10}	*Matta*, 2013
$CO_2^+ + NO \rightarrow NO^+ + CO_2$	1.23×10^{-10}	*Schunk and Nagy*, 2009
$CO_2^+ + O_2 \rightarrow O_2^+ + CO_2$	5.0×10^{-11}	*Barth*, 1985
$O^+ + N_2 \rightarrow NO^+ + N$	1.2×10^{-12}	*Matta*, 2013
$O^+ + O_2 \rightarrow O_2^+ + O$	2.1×10^{-11}	*Schunk and Nagy*, 2009
$O^+ + NO \rightarrow NO^+ + O$	8.0×10^{-13}	*Schunk and Nagy*, 2009
$O^+ + CO_2 \rightarrow O_2^+ + CO$	1.1×10^{-9}	*Matta*, 2013
$O_2^+ + NO \rightarrow NO^+ + O_2$	4.6×10^{-10}	*Schunk and Nagy*, 2009

586

587 **Figures**

Figure 1. (Left) The average altitude profiles of O_2^+, O^+, CO_2^+, and electron densities during a deep dip campaign from between April 17, 2015 to April 22, 2015. The green circles represent the average altitude profile of O_2^+, the blue circles represent O^+, and the red circles represent CO_2^+. O_2^+, O^+, and CO_2^+ densities are measured by NGIMS. The black circles are the electron density measured by the LWP instrument; the horizontal lines reflect the uncertainty. The solid lines with corresponding colors are the results from the 1D CAPIT simulation using the measured electron temperature as input. A Poynting flux of $\sim 3 \times 10^{-8}$ W/m^2 produces the best agreement between simulation and observations. (Right) The altitude profile of T_e used in the CAPIT simulation is derived from the measured electron temperature profile [from *Ergun et al.*, 2015]. The variability is $\sim$-0.1 eV to $\sim$0.5 eV from orbit to orbit (see Figure 4, *Ergun et al.*, 2015].
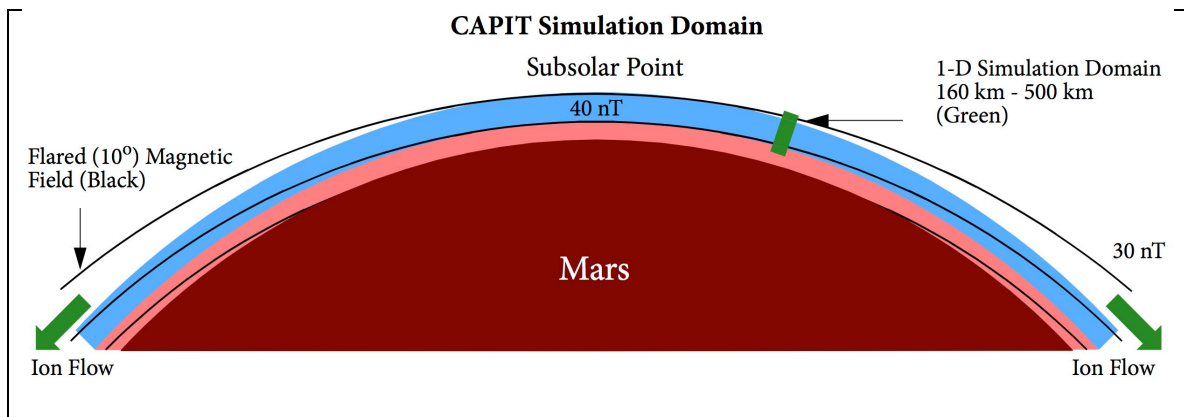
Figure 2. The simulation domain of the CAPIT model. The 2D CAPIT code includes the domain shaded in blue. The 1D CAPIT model, shaded in green, allows for motion along the draped magnetic field lines but no variation in the horizontal direction. The flare angle of the magnetic field is constant at 10°. The drawing is not to scale.
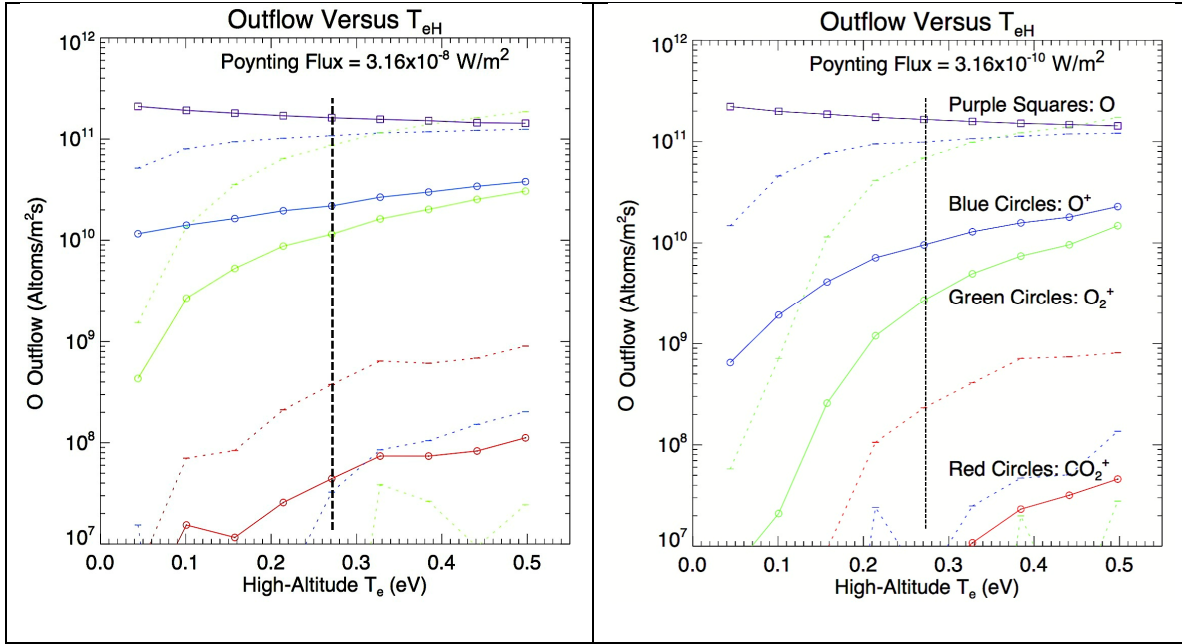
588

589

590

591

592

593

594

Figure 3. (Left) Estimated outflow versus high-altitude electron temperature from the 1D CAPIT code with weak pointing flux of 3.16×10^{-10} W/m^2. The purple squares and line represent the estimated outflow of O from dissociative recombination of O_2^+. The blue circles and line are the estimated outflow of O^+. Green represents O_2^+ and red represents CO_2^+. The dashed lines indicate the maximum outflow (F_{max}) and the minimum outflow (F_{min}). One can see a strong increase in O_2^+ outflow with increasing electron temperatures. Vertical dashed lines show measured average T_{eH}. (Right) Outflow versus T_{eH} with nominal values of low-frequency Poynting Flux (3.16×10^{-8} W/m^2). Outflow is larger at low electron temperatures due to the ion heating.
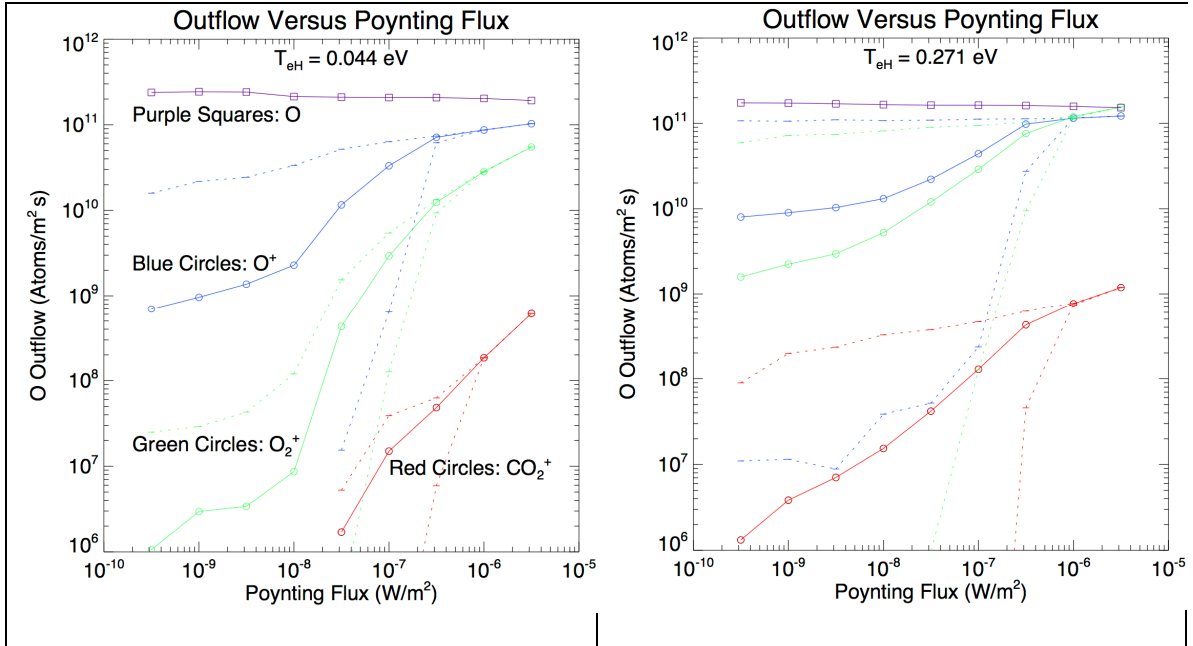
595

596

597

598

599

600

601

Figure 4. (Left) Outflow versus low-frequency Poynting flux (ion heating) from the 1D CAPIT code with low T_{eH} (0.044 eV). The purple squares and line represent the estimated outflow of O from dissociative recombination of O_2^+. The blue circles and line are the estimated outflow of O^+. Green represents O_2^+ and red represents CO_2^+. The dashed lines indicate the maximum outflow (F_{max}) and the minimum outflow (F_{min}). One can see a strong increase in O^+ and O_2^+ outflow with increasing low-frequency Poynting flux. (Right) Outflow versus low-frequency Poynting flux with nominal values of T_{eH} (0.271 EV). Outflow is larger at low electron temperatures due to the ambipolar electric field.

602

603
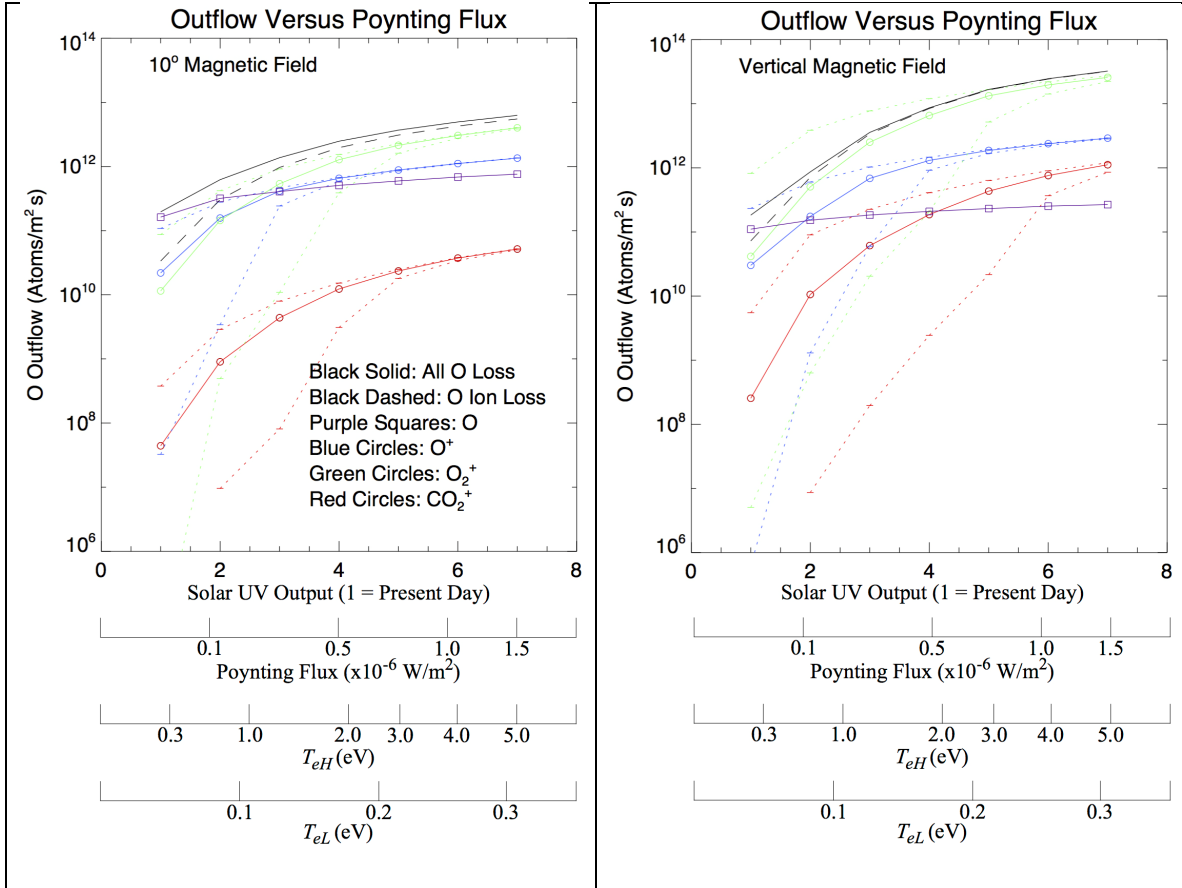
Figure 5. Outflow versus solar output. The color scheme is the same as in Figures 3 and 4. The Poynting flux increases as the square of the solar UV output and T_{eH} is increased as the solar output to the 3/2 power. The left panel has a draped magnetic field at 10°. The right panel has a vertical magnetic field. With the 10° magnetic field, ion outflow exceeds that of dissociative recombination by nearly an order of magnitude under strong solar UV fluxes and strong electron and ion heating. With a vertical magnetic field, ion outflow can reach values resulting in substantial atmospheric loss.

604

MAVEN Data and CAPIT Simulation

Circles:
o - n_e (LPW)
o - O_2^+ (NGIMS)
o - O^+ (NGIMS)
o - CO_2^+ (NGIMS)

Lines:
n_e (simulated)
O_2^+ (simulated)
CO_2^+ (simulated)
O^+ (simulated)
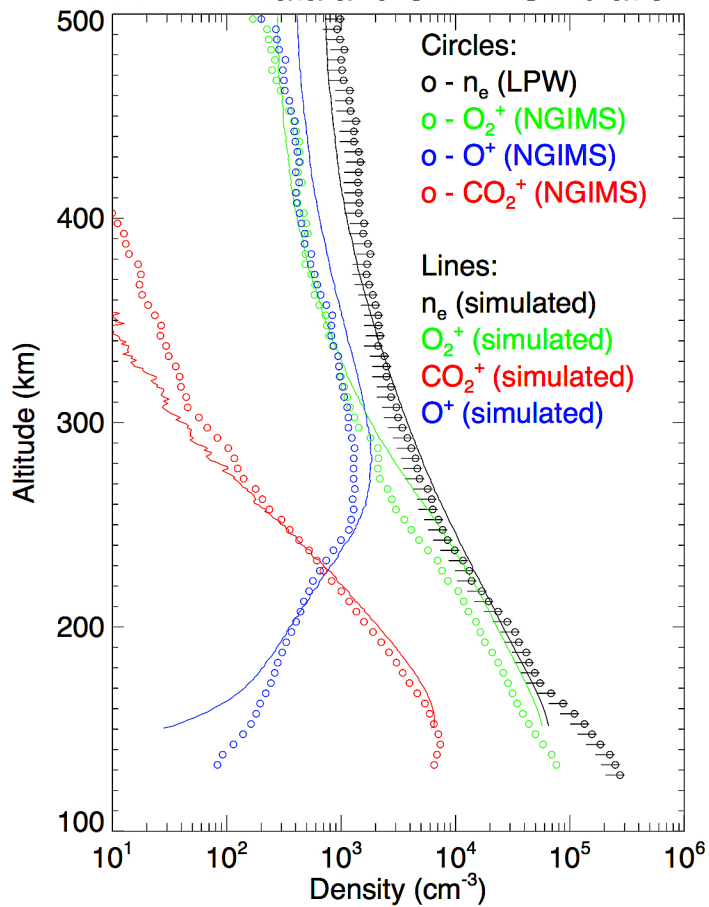
Analytic Form of T_e Profile

Black Circles: Mean T_e
Blue Line: Fit
T_L = 0.044 eV
T_H = 0.271 eV
Z_o = 241 km
H_o = 60 km
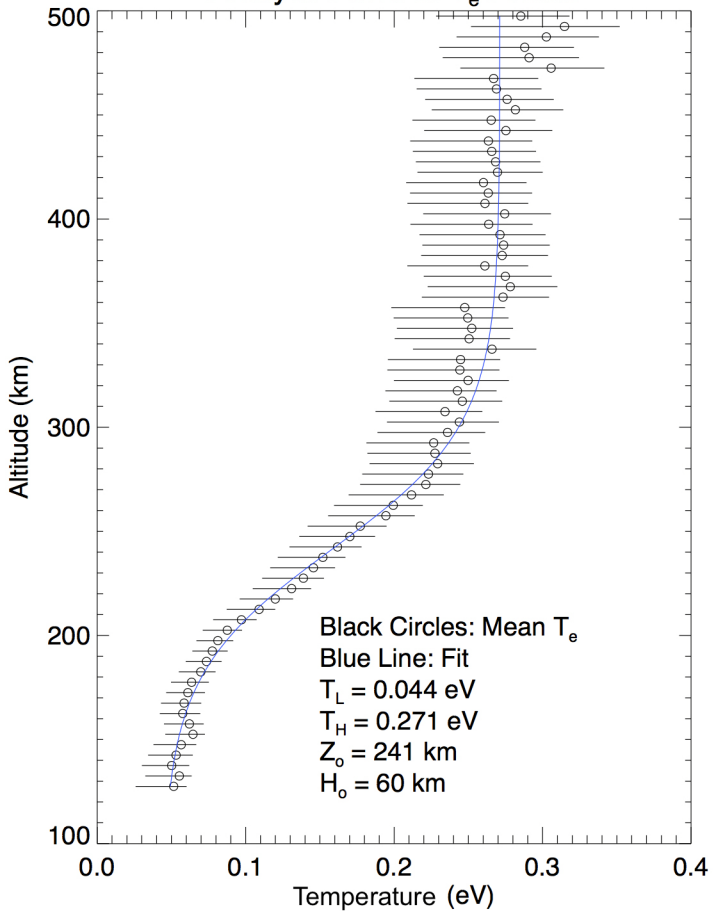
CAPIT Simulation Domain

Subsolar Point

40 nT

1-D Simulation Domain
160 km - 500 km
(Green)

Flared (10°) Magnetic
Field (Black)

Mars

30 nT

Ion Flow

Ion Flow

Outflow Versus T_{eH}

Poynting Flux = 3.16×10^{-10} W/m^2

Purple Squares: O

Blue Circles: O$^+$

Green Circles: O$_2^+$

Red Circles: CO$_2^+$

Outflow Versus T_{eH}

Poynting Flux = 3.16×10^{-8} W/m^2

O Outflow (Altoms/m^{2}s)

High-Altitude T_e (eV)

Outflow Versus Poynting Flux

$T_{eH} = 0.044$ eV

Purple Squares: O

Blue Circles: O^+

Green Circles: O_2^+

Red Circles: CO_2^+

O Outflow (Atoms/m^2 s)

Poynting Flux (W/m^2)

Outflow Versus Poynting Flux

$T_{eH} = 0.271$ eV

O Outflow (Atoms/m^2 s)

Poynting Flux (W/m^2)

Outflow Versus Poynting Flux

10° Magnetic Field

Black Solid: All O Loss
Black Dashed: O Ion Loss
Purple Squares: O
Blue Circles: O^+
Green Circles: O_2^+
Red Circles: CO_2^+

O Outflow (Atoms/m² s)

Solar UV Output (1 = Present Day)

Outflow Versus Poynting Flux

Vertical Magnetic Field

O Outflow (Atoms/m² s)

Solar UV Output (1 = Present Day)